

Article

A Numerical Study on an Oscillating Water Column Wave Energy Converter with Hyper-Elastic Material

Xiang Li  and Qing Xiao * 

Department of Naval Architecture, Ocean and Marine Engineering, University of Strathclyde, Glasgow G40 LJ, UK

* Correspondence: qing.xiao@strath.ac.uk

Abstract: A model different from the traditional WEC, known as the flexible wave energy converter (fWEC), is numerically modeled in this paper. The fWEC is believed to be more efficient and has a greater range of operation when compared with the conventionally rigid WEC. A fully coupled fluid–structure interaction (FSI) tool is developed for the research performed in this paper. This tool is able to accommodate the dynamic interaction between the flexible membrane structure of the fWEC and the surrounding fluid. In this research, both linear-elastic and hyper-elastic materials are examined for their use in the fWEC. The fluid flow surrounding the fWEC is solved by a computational fluid dynamics (CFD) method. The deformation of the hyper-elastic structure within the fWEC is modeled using a finite element analysis method (FEA). Both the hyper-elastic material of the fWEC and the free surface wave contribute to the overall nonlinearity of the numerical simulation. To tackle this problem, a robust coupling scheme is implemented by an advanced coupling library. With this tool, the flexible deformations within the fWEC structure can be accurately captured. The degree of these deformations can then further be examined, allowing the overall effects on the fWEC energy output to be determined. The simulation results show that the peak deformation of the hyper-elastic material is four times that of the linear-elastic material. This suggests that the fWEC would perform better and generate greater power using the hyper-elastic material compared with the linear-elastic material. Additionally, because a wide range of wave conditions are studied, it can be concluded that unlike conventional WECs, the efficiency of energy harvesting of such an fWEC is not sensitive to certain wave periods. Such findings are supported by both the detailed flow fields captured and the structural stress–strain analysis results from this simulation.

Keywords: flexible WEC; CFD; hyper-elastic material; fluid–structure interaction



Citation: Li, X.; Xiao, Q. A Numerical Study on an Oscillating Water Column Wave Energy Converter with Hyper-Elastic Material. *Energies* **2022**, *15*, 8345. <https://doi.org/10.3390/en15228345>

Academic Editor: Eugen Rusu

Received: 6 October 2022

Accepted: 3 November 2022

Published: 8 November 2022

Publisher's Note: MDPI stays neutral with regard to jurisdictional claims in published maps and institutional affiliations.



Copyright: © 2022 by the authors. Licensee MDPI, Basel, Switzerland. This article is an open access article distributed under the terms and conditions of the Creative Commons Attribution (CC BY) license (<https://creativecommons.org/licenses/by/4.0/>).

1. Introduction

In order to achieve the carbon emission reduction targets set in recent years, many countries have implemented different policies in an effort to increase their usage of renewable energy. Additionally, the oil and gas shortage in 2022 as a result of the Ukraine crisis highlighted the issues of reliance on a single source of energy. Wave energy technologies are potential sources of clean energy which have already been studied over the past few decades. Many classic wave energy converter (WEC) prototypes have already been invented, rigorously tested, and developed fully (e.g., Pelamis Wave Power [1] and Aquamarine Power Oyster) [2]. Despite this, only a limited number of prototypes have reached the economic validation stage (a few devices have undergone long-term sea trials), and no WECs have been successfully used at a large commercial scale. This may be due to several inherent challenges associated with traditional WECs. One such challenge stems from the issue that many WECs are mechanically complex through the use of multiple subcomponents (e.g., the Albatern 12S Squid WEC) [3]. These structures significantly reduce the durability and stability of the WEC while also increasing manufacturing and

maintenance costs. Another issue of traditional WECs is their poor adaptability to the ocean wave conditions where they are installed.

For an oscillating water column (OWC) WEC [4], the resonant phenomenon is very important for maximizing power generation. This type of resonance is usually caused by the nonlinear air–water wave free surface interaction with a surface-piercing structure [5,6], which is similar to harbor oscillations or gap resonance [7,8]. Those WECs are only able to produce a considerable amount of power under a specific range of conditions (e.g., between a narrow range of ocean wave frequencies). If these conditions are not met, then the performance of the WEC will be significantly hindered and reduced.

One way to address the aforementioned reliability and survivability issues is to use flexible materials when constructing WECs. Deformable materials such as rubber and silicon elastomers can be widely used for different parts of the WEC, such as the power take-off system using dielectric elastomer (DE) materials (Moretti et al. [9]) or the primary mover of WECs [10].

A series of studies by Moretti [11,12] on the utilization of a DE material for an oscillating water column (OWC) device showed promising results and the effectiveness of constructing OWCs with DEGs. The experimental wave tank test indicated that a maximum fraction of 18% of the wave energy can be converted into electricity. Based on the experimental study, a surge OWC was developed and studied numerically with a simplified hydrodynamic model, aiming to identify an optimal control strategy to maximize the device's power production [13]. The results showed that the estimated power outputs can be as high as 1.5 MW if a 1.5 m³ elastomeric material is used.

With the recent developments of WECs utilizing flexible materials, a greater understanding of how WECs are affected by hydrodynamic forces is required, most importantly the forces experienced by the WEC substructures and the fluid-flexible structure–interaction phenomena linking to the material deformation or damage and direct power take-off. Currently, existing research on fWECs is limited, with studies using the numerical analysis tool providing limited information. These are either based on a reduced-order model or decoupled numerical modeling for fluid flow and structural deformation. The inherent disadvantage of these models is their lack of applicability for various types of fWECs, as the assumptions made in one device may not be valid for other models. In addition, these simplified models are inaccurate when the fluid nonlinearity and material nonlinearity become profound, and thus, the coupling between fluid flow and structure deformation must also be considered. A list of some typical works is given below.

A study conducted by Michailides [14] investigated the response of a flexible structure consisting of four rigid plates connected by constraints. The whole structure integrates the function of the breakwater and power take-off device. The investigation was based on the potential flow theory with the hypothesis of linearization and being inviscid and irrotational. Their results demonstrated a desirable amount of wave energy production by the WEC. Babarit et al. [15] studied a bulge wave WEC (i.e., SBM S3) constructed from DE material. A lumped parameter modeling system was combined with spectral decomposition and the potential flow theory. The Anaconda WEC is a model which has been extensively studied both experimentally and numerically [16,17]. Tube distensibility equations were utilized in the study to describe the deformation of the flexible tube. This one-dimensional model was originally developed to be tested under the simulation of the vascular system. Alongside this, a WEC rubber bag was tested using a combination of the potential flow theory and the boundary element method (BEM) [18]. Applying a distributed-parameter analytical approach, Renzi coupled the linear piezoelectric constitutive equations with the potential flow equations to cope with the free surface wave. A similar submerged piezoceramic plate WEC has also been extensively studied [19]. Lastly, Zheng et al. [20] studied the characteristic of a circular plate under regular waves, investigating the effect of varying radius and edge conditions on the performance of a circular plate.

A high-fidelity partitioned scheme that preserves all these desired features of the ideal WEC is paramount. This partitioned scheme relies on the data transferring between

the computational fluid dynamic (CFD) solver and the computational solid dynamics (CSD) solver to solve a coupled fluid–structure interaction (FSI) problem. King et al. [21] investigated the use of a partitioned scheme on the Bombora WEC. The CFD method was coupled with the finite element model in their study, and the simulation indicated the instability of the coupling process. For these issues to be solved, extremely small relaxation parameters are required, leading to a very large number of iterations (>100) to reach a convergent solution. The results of the coupled and uncoupled models show that they later underestimated the results by 25% compared with the coupled method. In our previous study, a two-dimensional simulation on the PolyWEC [11] was conducted with the use of a high-fidelity CFD method together with multi-body dynamics, creating a strong coupling strategy [22]. Even though a linear-elastic material was adopted, the nonlinear effect was overwhelmingly strong, and thus the simulation was unstable, requiring 50 iterations at each timestep for a convergent solution.

Aside from the aforementioned studies discussed, as far as the authors are aware, there has been no other successful analysis of fWECs using the high-fidelity CFD-FEA tool. The biggest challenge for such a simulation is the numerical stability problem, as mentioned before, which is mainly affected by the added mass of the flexible structure. The greater added mass seen in the fWEC destroys the stability of the coupling algorithm for modeling. Through theoretical analysis, it has been discovered that as the added mass entrained by the fWEC becomes greater, the stability of both the explicit and implicit coupling schemes reduces significantly [23]. This is just the case for the fWEC application, where the added mass is hundreds of times the mass of the flexible structure and therefore dominates the inertia of the fWEC system.

In this paper, the linear material model used in our previous study is extended to a hyper-elastic material, focusing with particular interest and importance on its practical application in fWECs. In this study, it is demonstrated that the use of hyper-elastic material can significantly improve the performance of an fWEC. Because the fluid–structure interaction induced by the hyper-elastic material is highly nonlinear, which makes convergence more difficult, previously used tools such as the multi-body dynamic tool or the coupling scheme in [22] are not applicable to this study. To solve this problem, a more versatile finite element method is introduced in this study. The coupling between the flow solver and structural solver is achieved by using the Precise Code Interaction Coupling Environment (preCICE), a coupling library for partitioned multi-physics simulations [24]. With this tool, the material selection and its influence on fWEC performance with different ocean wave conditions are examined, and the fWEC’s power output is estimated.

2. Numerical Method

For the fWEC, a strong fluid–structure interaction (FSI) problem needs to be solved, and thus a fully coupled FSI tool is developed to solve such problems. In particular, the fluid field is solved by a high-fidelity CFD solver, while the deformation of flexible bodies is solved using the FEA method. For data exchange between the two solvers at each time step, an open-sourced coupling library for multi-physics simulations is used.

2.1. Fluid Solver

The CFD solver is developed based on the multi-phase solver interFOAM provided in OpenFOAM [25]. The governing equations of this include the continuity equation and incompressible Navier–Stokes equations:

$$\nabla \cdot U = 0 \quad (1)$$

$$\begin{aligned} P \frac{\partial \rho U}{\partial t} + \nabla \cdot (\rho(U - U_g)U) = -\nabla P_d - g \cdot x \nabla \rho \\ + \nabla \cdot (\mu_{eff} \nabla U) + (\nabla U) \cdot \mu_{eff} + f_\sigma \end{aligned} \quad (2)$$

where U is the velocity of the fluid, ρ is the density, U_g denotes the speed of the motion of the mesh grid, which is zero for a fixed boundary, P_d denotes the dynamic pressure, g is the gravity acceleration, μ_{eff} denotes the effective dynamic viscosity, and f_σ is the surface tension, which is only considered on the free surface. The volume of fluid (VOF) method is used to capture the free surface [26]:

$$\frac{\partial \alpha}{\partial t} + \nabla \cdot ((U - U_g)\alpha) + \nabla \cdot (U_r(1 - \alpha)\alpha) = 0 \quad (3)$$

where α is the phase fraction denoting the form of the fluid, $\alpha = 1$ means the fluid is water, and $\alpha = 0$ means it is air. The fluid density and viscosity can also be described by phase fractions:

$$\rho = \alpha\rho_w + (1 - \alpha)\rho_a \quad (4)$$

$$\mu = \alpha\mu_w + (1 - \alpha)\mu_a \quad (5)$$

For numerical wave generation, the velocity is prescribed at the inlet boundary based on Stokes's second-order wave theory [27]:

$$u = \frac{\pi H}{T} \frac{\cos k(z+d)}{\sinh kd} \cos \theta + \frac{3\pi H}{4T} \left(\frac{\pi H}{L} \right) \frac{\cos 2k(z+d)}{\sinh^4 kd} \cos 2\theta \quad (6)$$

$$w = \frac{\pi H}{T} \frac{\sinh k(z+d)}{\sinh kd} \cos \theta + \frac{3\pi H}{4T} \left(\frac{\pi H}{L} \right) \frac{\sinh 2k(z+d)}{\sinh^4 kd} \sin 2\theta \quad (7)$$

2.2. Structural Solver

The deformation of the flexible structure is solved by an open-sourced FEA code named Calculix [28]. This code has been successfully coupled with our in-house flow solver and is widely used for a variety of biomimetic fish swimming problems involving passive flexible material deformation [29–31]. The governing equation of the structure solver is the weak form of the balance of momentum and is written in the differential form:

$$\rho_s \frac{D^2 U_s}{D^2 t^2} = \nabla \cdot P_s + \rho_s f_s \quad (8)$$

where the acceleration of the material point is obtained by the second derivatives of the displacement vector U_s of the structure and surface forces are modeled by the second Piola–Kirchhoff stress tensor P_s , while the body force per unit mass, such as gravity, is represented by f_s .

A constitutive equation describing the relation between the stress and the strain is used to close Equation (8). Specifically, for a Saint Venant–Kirchhoff material, the second Piola–Kirchhoff stress tensor P_s is obtained by

$$P_s = C : E, E = 1/2(F^T F - \delta) \quad (9)$$

where C is the elasticity tensor, E represents the Green–Lagrange strain tensor, the deformation gradient is characterized by F , and δ is the unit tensor. The governing equation of the structure of Equation (8) is discretized using the finite element method. With the application of the virtual work method, a linear algebraic equation system by discretization in the complete solid domain is obtained:

$$[K]\{U_s\} + [M]\frac{D^2}{Dt^2}\{U_s\} = \{F\} \quad (10)$$

where $[K]$ is the global stiffness matrix, $[M]$ is the global matrix, and $\{F\}$ is the global force vector. The time domain is discretized using the α method [28].

2.3. Coupling Scheme

The coupling method between the CFD and CSD solver is introduced. In this study, an open-sourced code named preCICE which functions as a general framework for partitioned method studies, is utilized [28,32]. It provides a tool which minimizes the effort of adapting the original computation code when coupling two solvers, as well as several schemes to accelerate and stabilize the coupling process.

It is very challenging to solve strongly coupled FSI problems, where numerical instabilities may cause divergence, especially when the fluid has a similar density to the solid structure [23]. This problem is especially serious when the nonlinearity is strong, such as for the hyper-elastic material study in this paper. In order to achieve numerical stability and convergence within this framework, a sub-iteration is added during each time step in an implicit scheme. In addition, the interface quasi-Newton method with an inverse Jacobian from a least squares model (IQN-ILS) [33,34] implemented in preCICE is used to stabilize the coupling and accelerate the convergence. This is a Newton–Raphson scheme that tries to find the root of the residual equations of the displacements and fluid forces at the interface. Since the fluid and structural grids are nonconforming, an interpolation between the two is needed to map the data at the interface. In this work, radial basis function (RBF)-based interpolation [35] is utilized, which is a data mapping method used in multi-physics coupling with the second-order method to transfer forces from the fluid solver to the structural solver and the deformation in turn, as shown in Figure 1.

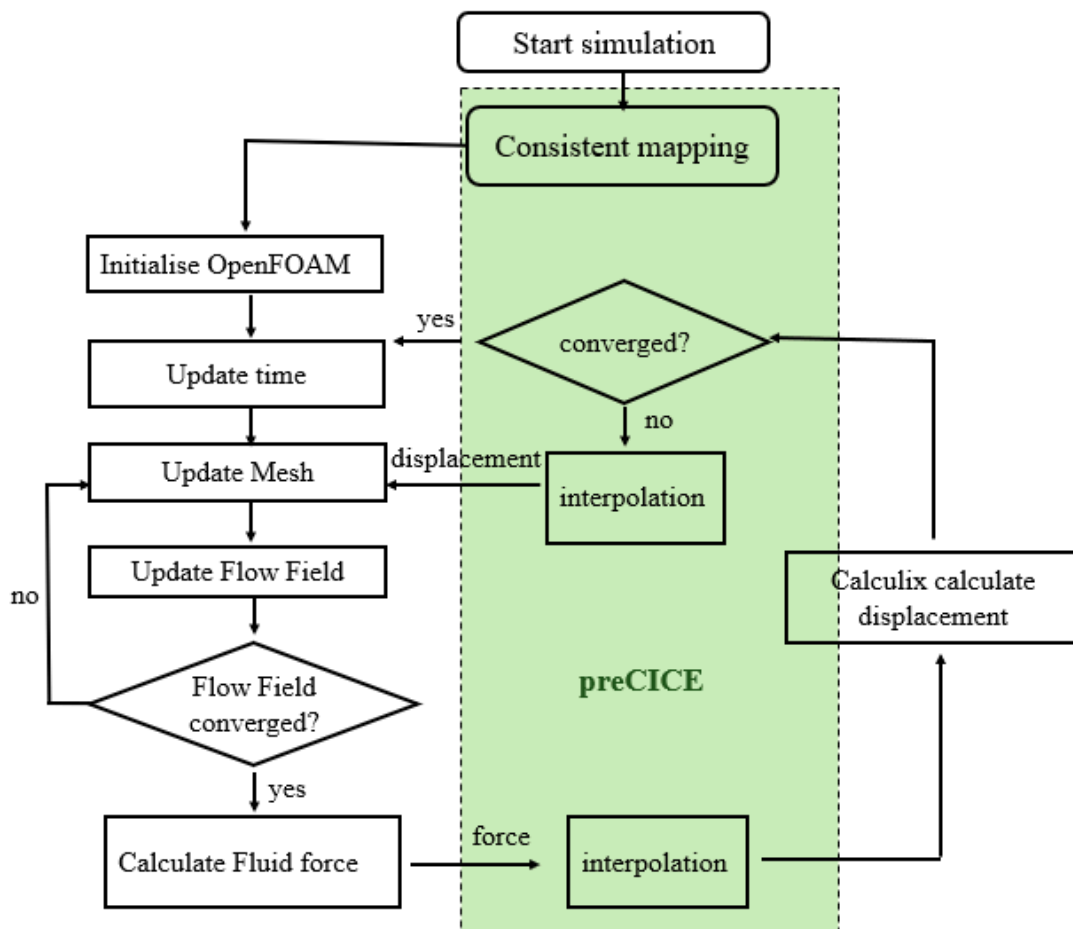


Figure 1. Model description.

The fWEC model studied was inspired by the PolyWEC device by Giacomo et al. [11]. The three-dimensional fWEC holds a symmetric geometry, whose section along the y axis is shown in Figure 2, where the origin is in the center of the initial membrane position. Here, x points in the wave's direction, and z opposes gravity's direction. The whole device is submerged under water, where the membrane made up of DEG material is the main element functioning as the PTO to convert the wave energy into electricity. The membrane is placed in the center of the device as an interface to separate the top water and bottom air chambers. The air pressure is almost constant and equal to the atmospheric pressure in the air chamber. A collector is attached at the top of the membrane, which aims to increase the added mass of the fWEC system. When a wave comes over, the pressure difference between the top and bottom surfaces of the membrane causes it to deform continuously as a balloon would. In this process, the membrane is stretched, thus leading to a change in thickness. The DE membrane holds stretchable electrodes on both faces and functions as a variable capacitor. Deformations induced by the hydrodynamic pressure cause a variation in the membrane's surface and thickness, hence leading to variations in the DEG capacitance. By properly modulating the voltage applied on the DEG as a function of the current deformation (e.g., allowing a charge on the DEG during the phases in which its capacitance decreases and keeping it uncharged while its capacitance is increasing), this allows converting part of the input mechanical energy into electrical energy [11].

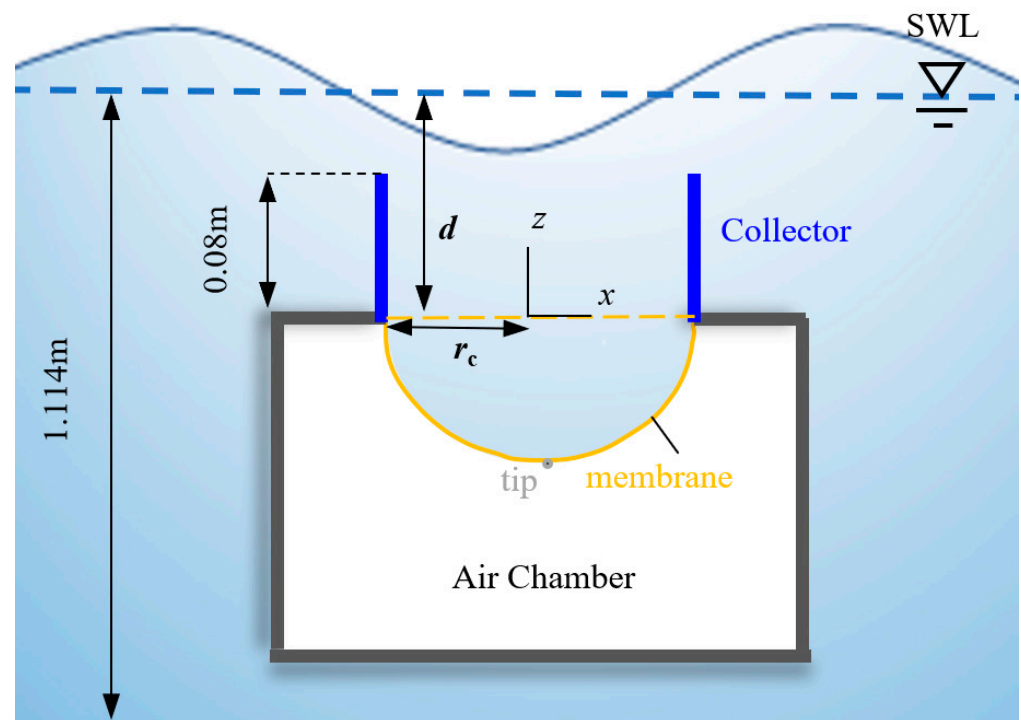


Figure 2. Sketch of the fWEC model. The plates in blue are given the name of the collector to create a water column above the membrane. The yellow solid line denotes the membrane which functions as the PTO. The yellow dashed line denotes the initial position of the membrane (unstretched).

A preliminary test shows that for three-dimensional numerical modeling, because of its highly nonlinear feature, a time step as small as 0.006% of the wave period is needed to ensure the stability of the simulation, which is very computationally expensive. To reduce the overall computational cost, the fWEC in this study is simplified into two dimensions.

In our numerical study, the geometric dimensions of the above device were designed based on experimental research [11], where the model was scaled down at a factor of 1:40/1:50. At the beginning, the membrane was unstretched with a radius of $r_c = 0.065$ m, and its initial position is shown in Figure 2. Once it started deforming, we monitored the

tip displacement of the membrane z_{tip} , which was directly linked to energy conversion. The distance between the position of the unstretched membrane and the static water level (SWL) was defined as the water height d .

The numerical wave was generated using Stokes second-order waves, as defined by Equations (6) and (7). The wave height was $H = 0.1$ m, and the selected wave periods were from 0.8 s to 1.8 s, corresponding to an unscaled fWEC operating with a wave period of 5.6–12.6 s for the real sea states.

The mesh configuration is shown in Figure 3, with a cell numbers of around 68,000. As shown in Figure 3a,b, the mesh was refined near the free surface and inside the collector to better capture the wave profile and the flow details. The boundary condition of the membrane was set up as a non-slip wall boundary for the fluid velocity and a zero gradient for the pressure. The velocity and pressure at the inlet boundary were prescribed by regular wave theory, and both were set to be zero gradients at the outlet boundary.

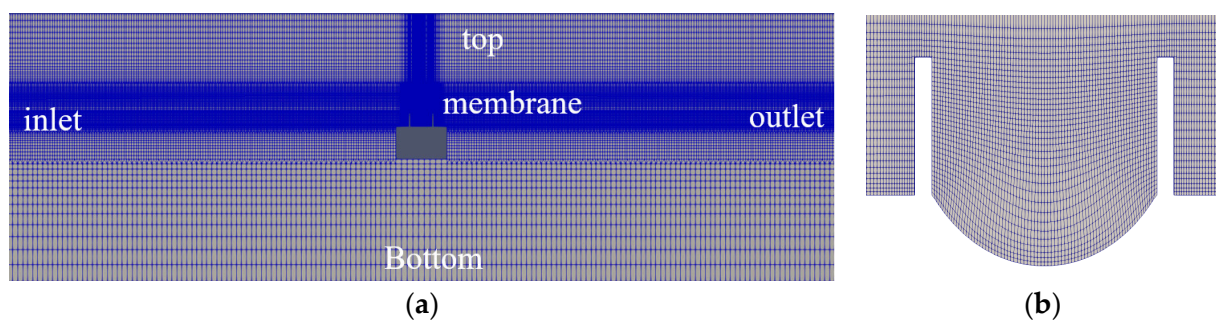


Figure 3. CFD mesh (a) of whole wave tank and (b) inside the collector with a deformed membrane.

To solve this time-dependent problem, the time step for all cases was fixed to 5×10^{-5} s, which was 0.006% T when $T = 0.8$ s. The pressure-velocity coupling was achieved through the PIMPLE (a combination of PISO and SIMPLE) algorithm. A second-order Crank–Nicolson scheme was used for temporal discretization. A second-order upwind scheme was adopted for convective terms. Gradient terms were handled via a second-order cell-limited Gauss linear scheme.

3. Results and Discussion

3.1. Grid and Time Step Sensitivity Study and Numerical Method Validation

The independence study for the mesh and time step was tested for an fWEC with $d = 0.18$ m, $H = 0.1$ m, and $T = 0.8$ s. Figure 4 shows the time-dependent deformation of the membrane z_{tip} with different mesh refinement and time steps. The surface mesh size of the base mesh was 1.25% of the characteristic length L (length of the membrane), which was 0.75% and 2% for the fine and coarse meshes, respectively. As indicated by Figure 4, the results from the base and fine mesh were very similar to each other, and therefore, the base mesh was selected to reduce the computational cost. As for the time step, there was no obvious difference observed. However, a large time step may cause the simulation to diverge. A comprising time step of 5×10^{-5} s was finally chosen for the rest of the simulation in this work.

To conduct numerical method validation, two cases were selected. The first case was a flow across a flexible cantilever plate behind a square cylinder. This was used to validate our developed tool for the fluid-flexible structure interaction, which was one of the key elements for this fWEC analysis. The second case was the numerical modeling for a rigid WEC under regular wave conditions.

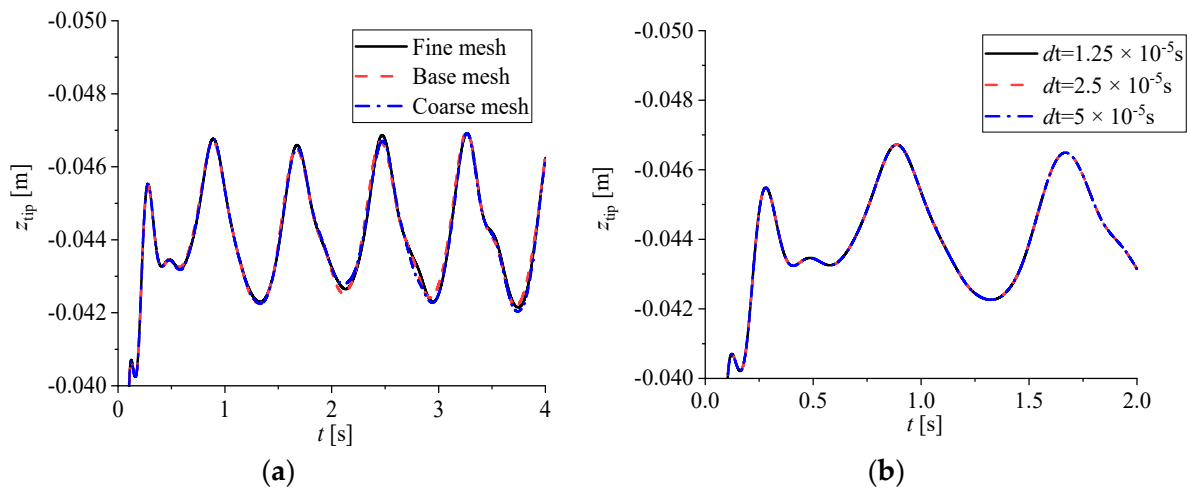


Figure 4. Time histories of the tip displacement with different (a) mesh densities and (b) time steps for a case of $d = 0.18$ m, $H = 0.1$ m, and $T = 0.8$ s.

The first case consisted of a fixed square bluff body, behind which Von Karman vortex street shedding occurred and excited a periodic deformation of the elastic cantilever, as seen in Figure 5a. The typical parameters were a Reynolds number Re of 330, a mass ratio m^* of 1.27, a non-dimensional bending stiffness K of 0.23, and Poisson's ratio ν of 0.35. The predicted time-dependent displacement of the tip of the beam is shown in Figure 5b. The frequency was estimated to be 3.137 Hz, and the amplitude of the oscillation was 1.071 cm, which are consistent with the other results summarized in Table 1.

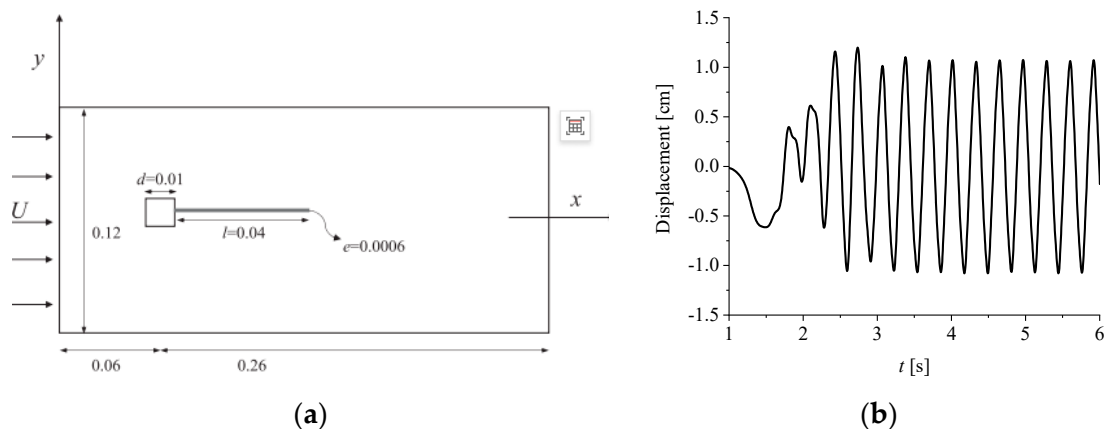


Figure 5. (a) The layout of the computational domain. (b) Displacement of the tip of the cantilever beam.

Table 1. Comparison of present results with the open literature.

Author	f (Hz)	Displacement (cm)
Matthies and Steindorf [36]	3.13	1.18
Wood et al. [37]	2.77–3.125	1.10–1.20
Walhorn et al. [38]	3.14	1.02
Habchi et al. [39]	3.25	1.02
Present	3.137	1.07

In the second case, a conventional rigid WEC was examined in our previous study, in which the numerical modeling of a wave–structure interaction problem was very well

validated against the results from wave tank testing [3]. In this problem, the WEC was made up of four floats with rigid connections in between. The incident waves came from the left side (see Figure 6a), having a wave height of 1.5 m and a wave period between 9.5 s and 10.5 s. The CFD modeling results, in terms of pitch motion responses, were in very good agreement with the experiment (see Figure 7).

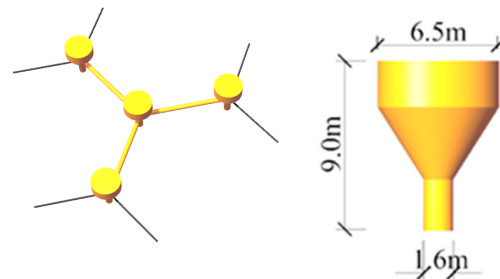


Figure 6. Sketch of the WEC model (from [3]).

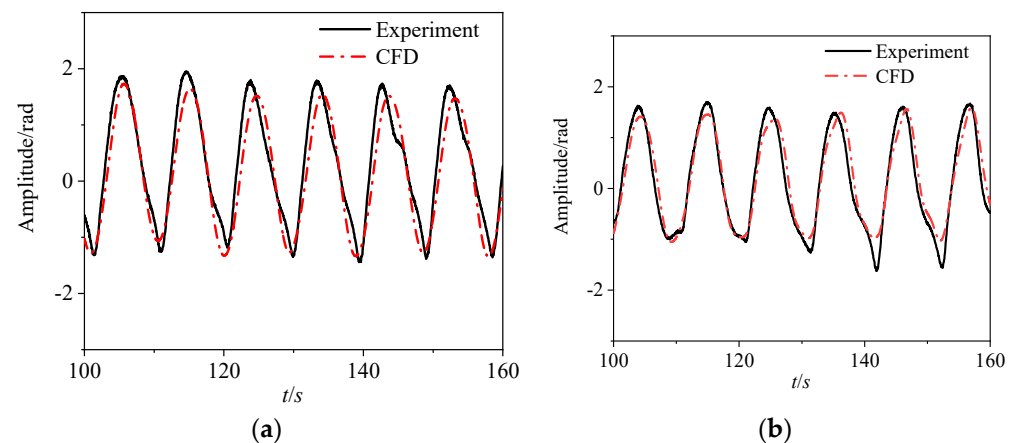


Figure 7. Pitch motion response of the floats in the middle with (a) $H = 1.5$ m and $T = 9.5$ s as well as (b) $H = 1.5$ m and $T = 10.5$ s (from [3]).

3.2. Role of Hydrostatic and Hydrodynamic Pressure on the Membrane's Deformation

In this study, the free surface was still and not disturbed at first, and the membrane started from a flat configuration. The motion response of the membrane could be divided into two phases. In phase one, the waves had not yet reached the structure, and the deformation of the membrane was driven by the hydrostatic pressure. After that, the membrane reached its equilibrium configuration and stopped deforming at a position of δ_{static} (see Figure 8). In phase two, the membrane moved periodically with waves passing by, induced by the hydrodynamic pressure. Within one wave period, the membrane oscillated with an amplitude of δ_{dynamic} . Since the magnitude of δ_{dynamic} was directly linked to the energy conversion, it was desirable to achieve a large value of δ_{dynamic} . Obviously, the fWEC system's structural natural frequency was determined by the material characteristics and the hydrostatic pressure, which was mainly contributed by the added mass of water inside the collector and thus the water height (d in Figure 2). However, in phase two, the dynamic motion of the membrane was also controlled by the wave states. In the following sections, the membrane deformation under a range of hydrostatic pressures is examined first to identify the system's natural frequency, followed by an investigation of the material characteristics and wave conditions' impact on the fWEC.

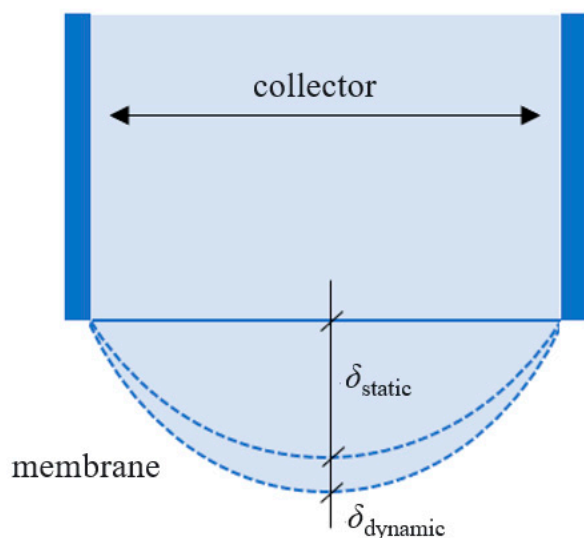


Figure 8. Membrane deformation under static pressure and dynamic pressure.

3.3. Response of Membrane Deformation under Hydrostatic Pressure

The tip displacement of the membrane under constant hydrostatic pressure (i.e., a constant $d = 0.18$ m) is illustrated in Figure 7, with the material properties being summarized in Table 2. The material’s hyper-elastic characteristics are described by the following strain energy potential equations [40], inspired by the rubber used in the fWEC:

$$E = \sum_{i=1}^N C_{i0} \left(\bar{I}_1 - 3 \right)^i + \sum_{i=1}^N \frac{1}{D_i} (J - 1)^{2i} \tag{11}$$

where I_1 is the Cauchy–Green deformation tensors and C_i and D_i are material constants. From zero, the hyper-elastic membrane held a larger displacement (z_{tip}) and a smaller frequency of motion than that of a linear-elastic material. The final equilibrium position of the membrane was $z_{tip} = -0.041$ m and $z_{tip} = -0.045$ m for the linear-elastic and a hyper-elastic material, respectively.

Table 2. Parameters for membrane materials.

	Young’s Modulus	Poisson’s Ratio	
Linear	6.5×10^5	0.35	
	(YEOH) C10	C20	C30
Hyper-Elastic	2.5×10^5	-1.3×10^5	5×10^4

The flow velocity field distributions inside the water collector with a hyper-elastic material at each sampling time from t_1 to t_6 in Figure 9 are shown in Figure 10. As revealed from those two figures, under a static pressure generated by a water height $d = 0.18$ m, at $t = t_1$, the membrane deformed downward from a flat configuration and reached its maximum displacement of z_{tip} . Afterward, it bounced back at $t = t_2$. The process repeated from $t = t_1$ to $t = t_6$ until the membrane reached its final stationary position. A pair of symmetric eddies can be observed in the water chamber which grew with time.

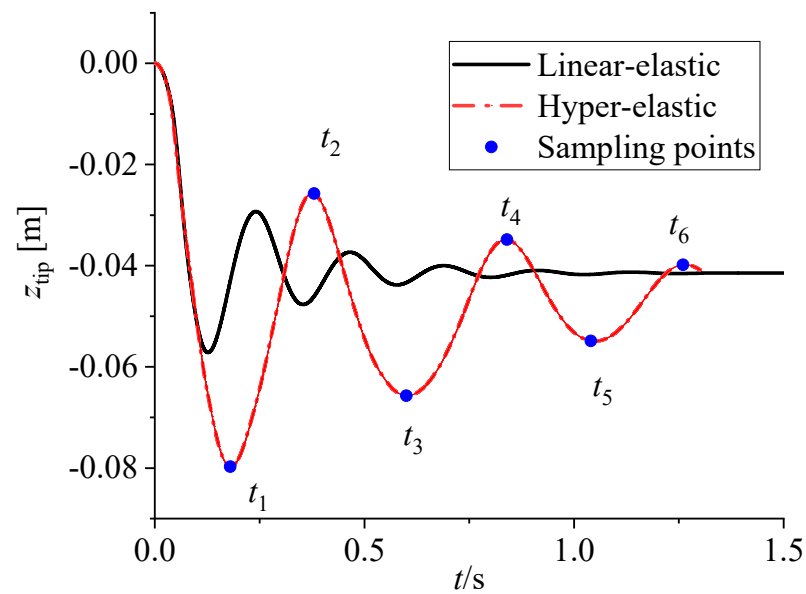


Figure 9. Tip displacement of the membrane with linear and hyper-elastic materials ($d = 0.18$ m).

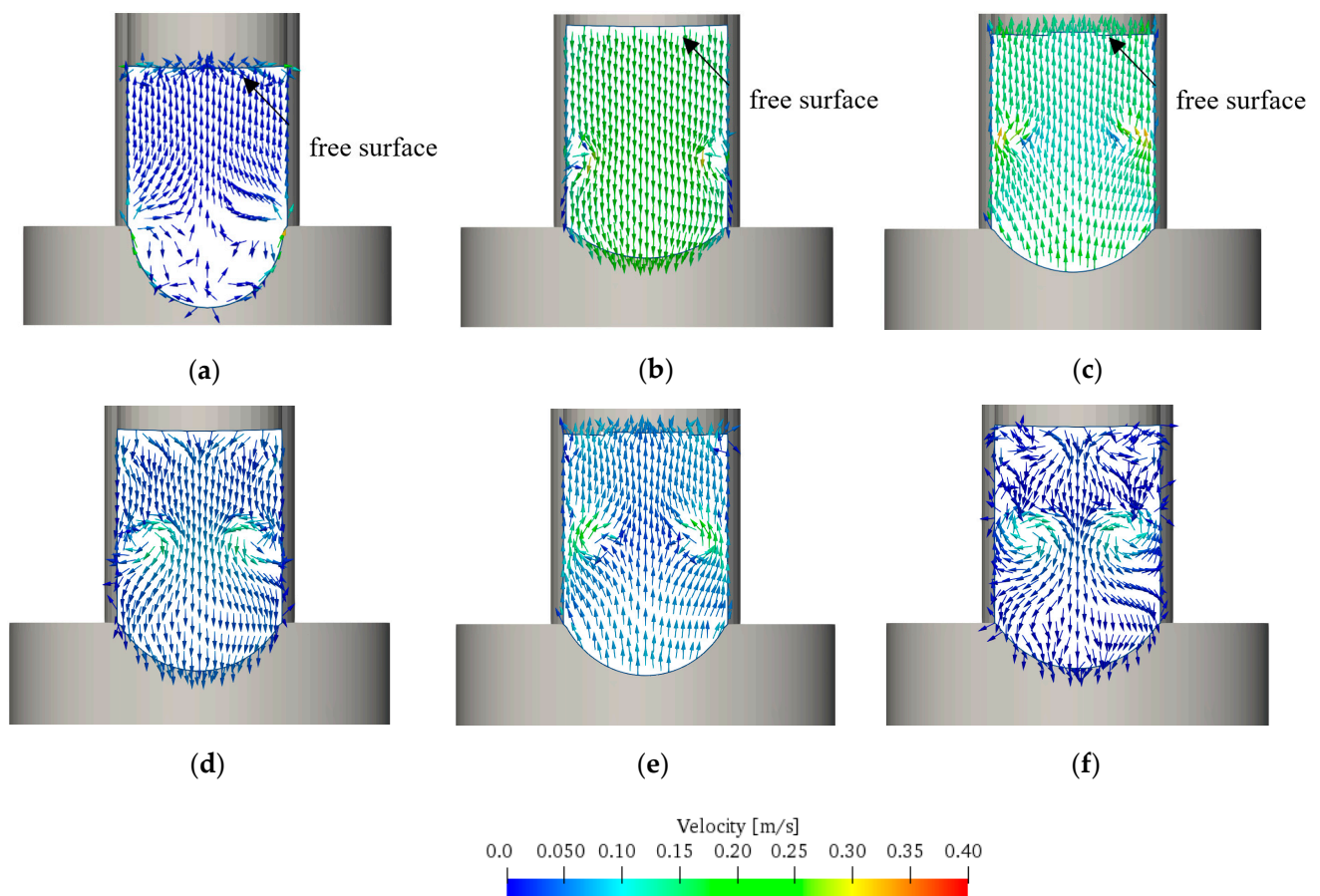


Figure 10. Development of the membrane deformation and the flow velocity vector inside the water chamber with a hyper-elastic material ($d = 0.18$ m): (a) $t = t_1$, (b) $t = t_2$, (c) $t = t_3$, (d) $t = t_4$, (e) $t = t_5$, and (f) $t = t_6$.

As mentioned earlier, the system's natural frequency is dependent on the water column height d (i.e., the added mass of the fWEC), where a series of cases was tested with variable

d values. The selection of d was based on the water height d_0 and a wave amplitude A of 0.05 m in an experimental model [11], resulting in a range of $d = d_0 \pm A$ in this study. Figure 11a,b shows the FFT analysis distributions for the tip displacement with variable d values for a linear-elastic and a hyper-elastic material, and their quantitative values are plotted in Figure 11c. In Figure 11a,b, it can be seen that given the same range of d variation, the dominant frequency of a linear-elastic material system occurred at 4.5 Hz, while that for a hyper-elastic material system was spread out in a range from 2.25 to 4.25 Hz. In addition, a second-order low frequency was also excited with large d values. This might have been caused by the strong nonlinearity associated with large d values. All the natural frequencies of the fWEC were out of the range of the wave frequencies ($f = 0.65\text{--}1.25$ Hz), which will be further discussed in Section 3.5.

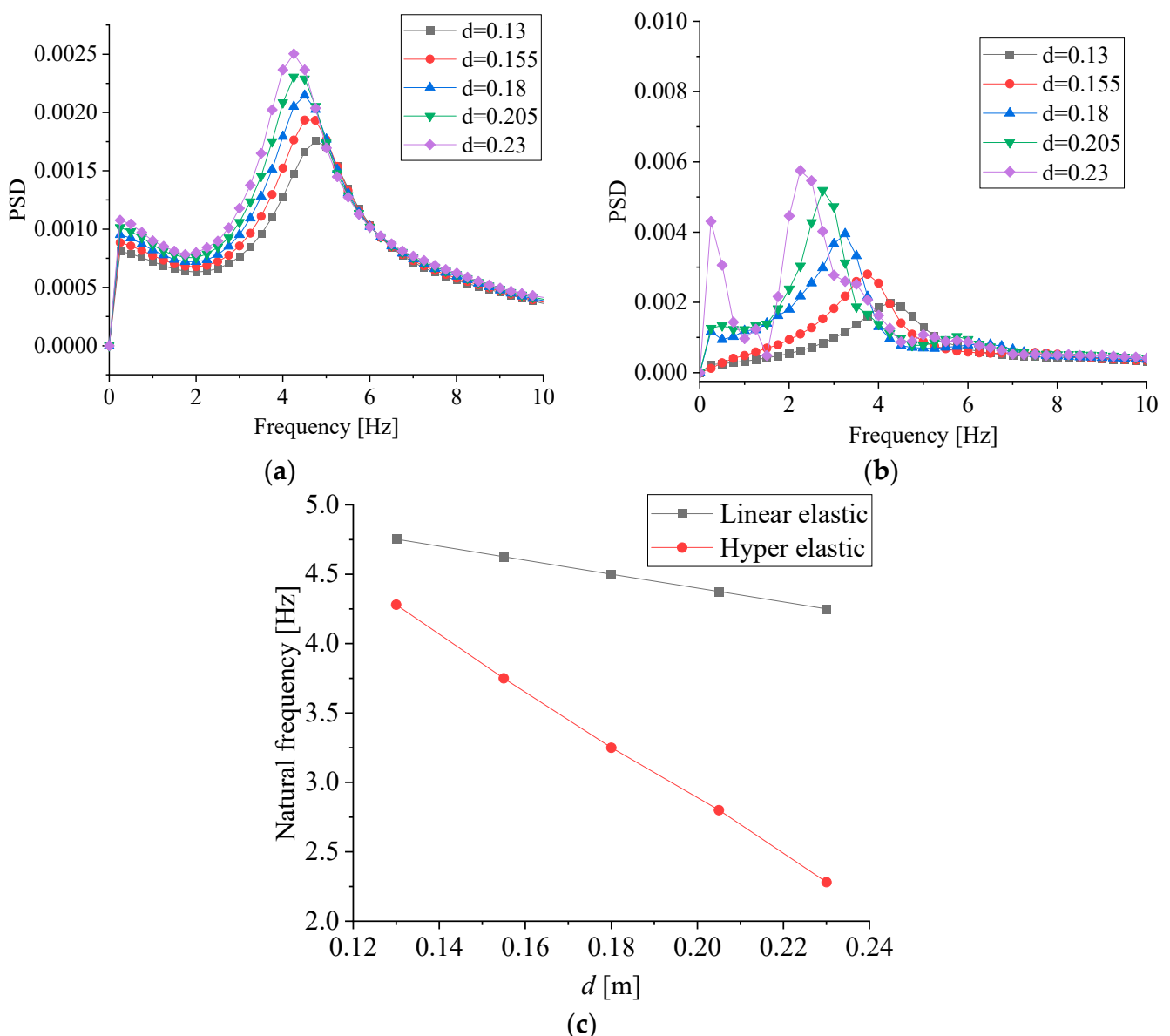


Figure 11. FFT analysis of the displacement with different d values for (a) linear-elastic material and (b) hyper-elastic material. (c) The natural frequencies via FFT analysis.

Figure 12a also indicates that the larger the added mass is, represented by larger d values, the smaller the fWEC's structural natural frequency is. Given the same added mass, the fWEC with hyper-elastic material presented a wider range of natural frequencies

than its counterpart with linear-elastic material. This is consistent with the classic natural frequency, defined as $\omega_n = \sqrt{k/m}$, where k is the stiffness and m is the mass. The tip displacement z_{tip} 's dependence on d is plotted in Figure 12. This shows that a hyper-elastic fWEC is easier to deform than a linear-elastic material, especially at large d values.

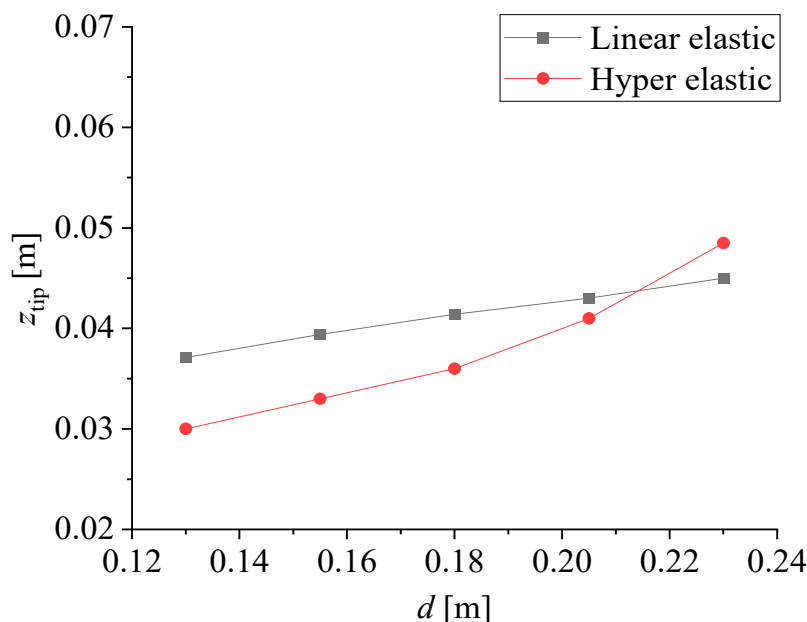


Figure 12. Tip displacement with different d values for linear-elastic and hyper-elastic materials.

3.4. Response of Membrane Deformation under Hydrodynamic Pressure: Material Impact

The dynamic response of fWECs with different materials under regular waves is discussed in this section. The wave height was fixed at $H = 0.1$ m, and the wave period T was $T = 0.8$ s for the convenience of analysis. In addition to the above two materials discussed in the last section (i.e., the linear-elastic and hyper-elastic M3), a softer hyper-elastic material M4 was also included. Their mechanical characteristic properties are listed in Table 3 below.

Table 3. Parameters for hyper-elastic materials.

	(YEOH) C10	C20	C30
M3	2.5×10^5	-1.3×10^5	5×10^4
M4	2.14×10^5	-1.14×10^5	4.29×10^4

The stress–strain relationship of the two materials in a uniaxial tensile test is shown in Figure 13, where the stress is represented by the Von Mises equivalent stress σ_{eq} . The curve is certainly linear for the linear-elastic material. For the hyper-elastic materials, the curves are divided into three sections, with two inflection points at the strain ε of 0.3 and 0.9. The materials appear to have had small stiffness values of $0.3 < \varepsilon < 0.9$ while having large stiffness values beyond this range, indicated by the large stress–strain curve slopes. For the fWEC in this study, it is obvious that the section between $\varepsilon = 0.3$ and $\varepsilon = 0.9$ is desirable to achieve a large deformation of the membrane and maximize the energy conversion.

The wave evolution and the dynamic response of the fWEC within half a wave period are shown in Figure 14. The wave crest propagated from the left and reached the device at $t = 3.85$ s. The water particle velocity magnitude increased and pointed to the surface normal direction of the membrane. This led to an increase in momentum and thus accelerated the deformation. Once the wave moved closer to the fWEC, the wave steepness increased, and the plunging wave broke afterward, which is a typical phenomenon associated with

a wave propagating with a sudden depth change. With a short delay, the deformation reached its maximum at $t = 3.95$ s. As the wave further propagated, the velocity gradually changed its direction upward. The wave, however, arrived at $t = 4.25$ s, and the membrane bounced back to its highest position with minimum deformation.

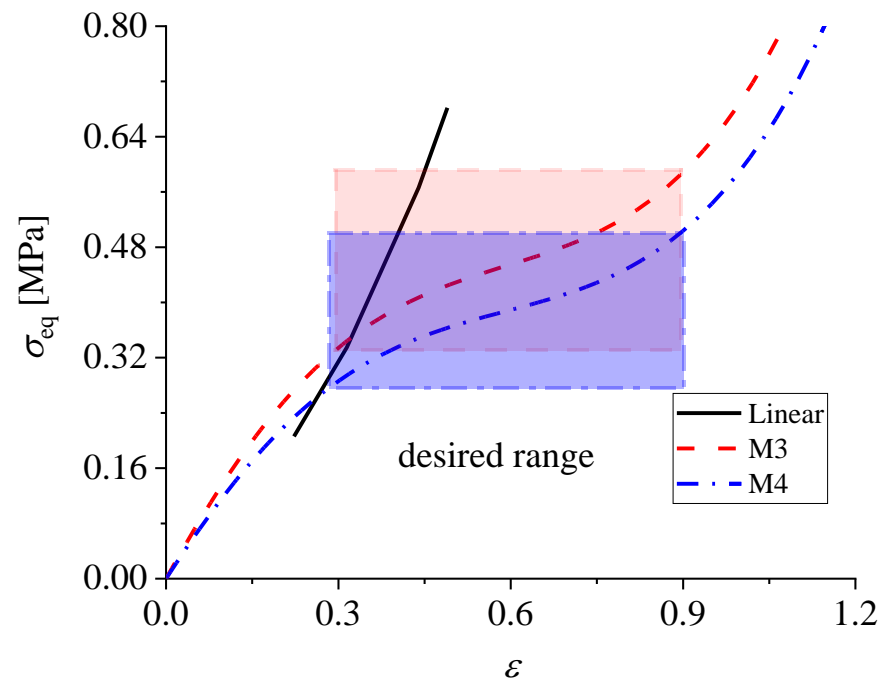


Figure 13. The stress–strain relationship of linear-elastic and hyper-elastic models M3 and M4, respectively.

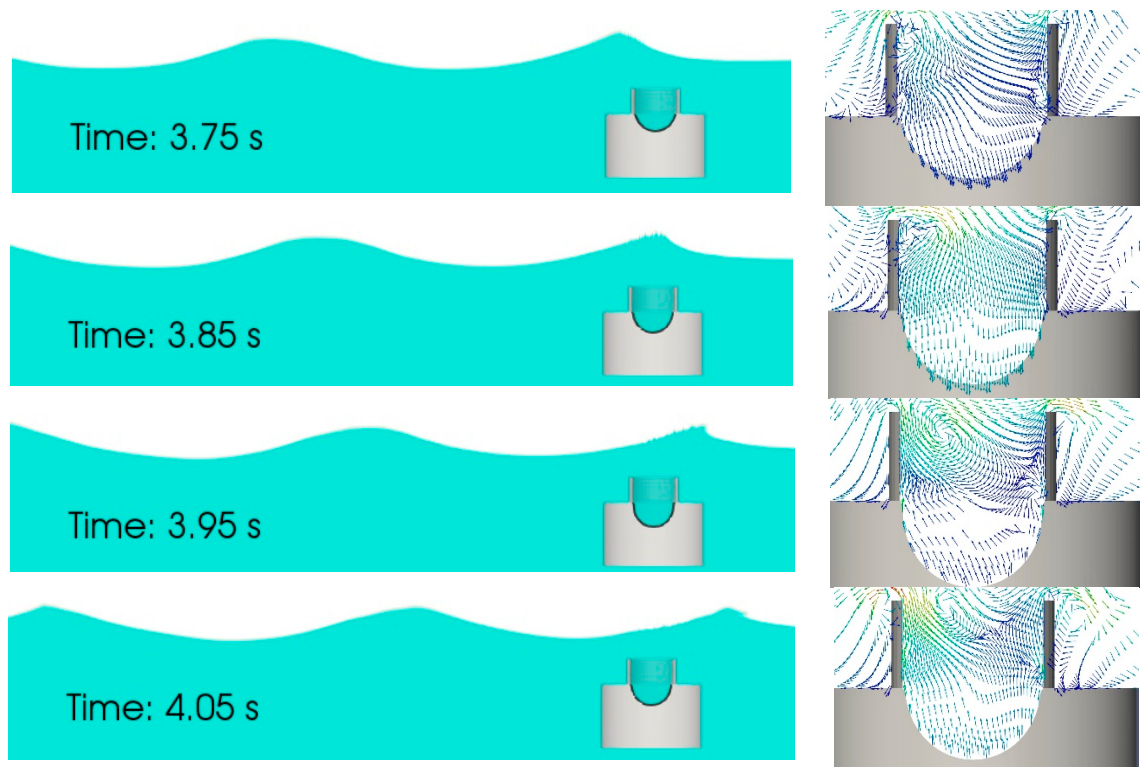


Figure 14. *Cont.*

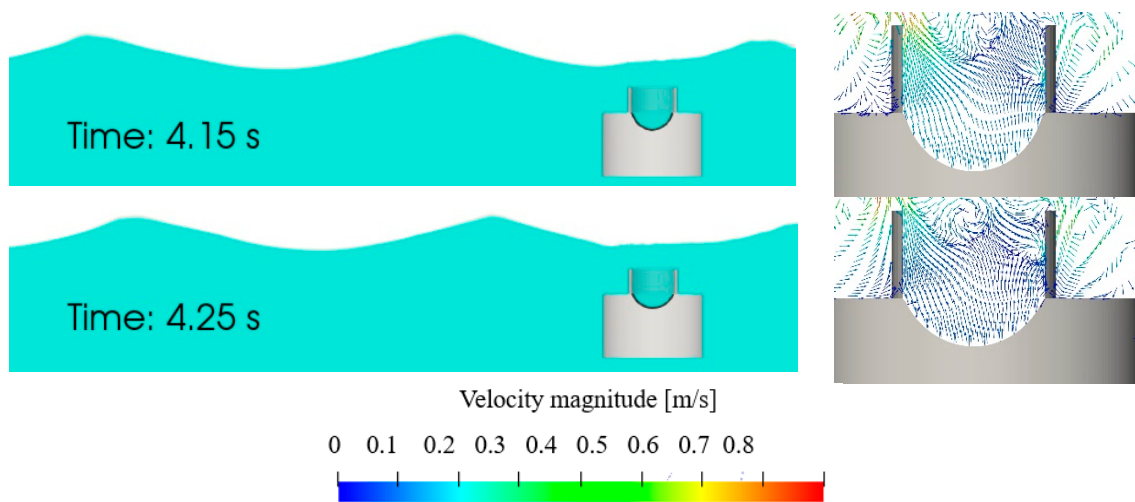


Figure 14. The evolution of the waves and fWEC response at different sampling times for M4, showing wave elevation (left) and zoomed-in view around the fWEC with velocity vectors (right).

The time history of the tip displacements for the linear-elastic, hyper-elastic M3, and M4 materials is shown in Figure 15. For the linear-elastic membrane and hyper-elastic M3 membrane, their initial equilibrium positions (δ_{static}) were similar under hydrostatic pressure. When waves propagated, although all three oscillated periodically with the same period as the waves, the motion of the M4 material was the largest among the three. The typical amplitudes were 0.0025 m for the linear-elastic material but 0.01 m for M3 and 0.0156 m for M4.

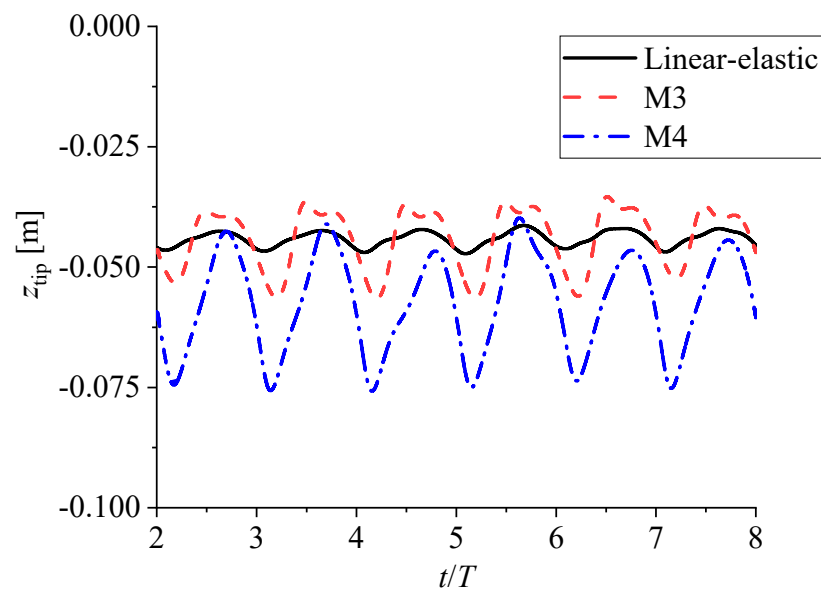


Figure 15. Tip displacement of the membrane with different materials ($H = 0.1$ m, $T = 0.8$ s, and $d = 0.18$ m).

It is worth mentioning that from our previous study on a linear-elastic material, a reduction in material stiffness only changed the initial equilibrium position δ_{static} and did not influence the motion-oscillating amplitude significantly [22]. In contrast, the present results show that a decrease in hyper-elastic material stiffness can achieve a profound increase in motion amplitude, indicating a distinct material characteristic between the linear-elastic and hyper-elastic material. In this regard, a hyper-elastic material provides a greater potential for deformation in contrast to a linear-elastic material.

Figure 16 shows the dynamic pressure contour around the fWEC. It can be seen that the dynamic pressure reached its maximum and minimum at the crest and wave trough, respectively. Inside the water chamber, the pressure was much larger than outside with the wave crest passing. The opposite was true when the wave trough passed over.

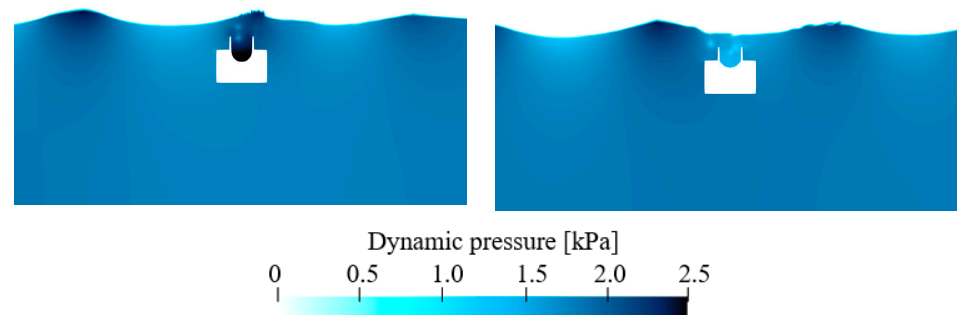


Figure 16. Dynamic pressure contours inside and outside the water chamber when the maximum (left) and the minimum (right) deformation were reached, respectively.

To better understand the membrane deformation in relation to the material stress induced by the hydrodynamic pressure, Figure 17 plots the instantaneous stress distribution along the membrane as well as the maximum and minimum membrane displacements. A comparison between the linear-elastic and a hyper-elastic M3 materials, displayed in Figure 17a,b, indicates that M3 had a larger deformation than the linear-elastic one, although their stress varied in the same range of $\sigma_{eq} = 0.21$ – 0.41 . This observation highlights the superiority of using a hyper-elastic material over using a linear-elastic material if a large displacement is desirable. Again, this was proven by the much softer material of M4 shown in Figure 17c. The time-dependent stress and strain variation at the tip of the membrane is shown in Figure 18a and b. This confirms the above findings from Figure 17, with some additional information added on the appearance of nonlinearity of the material associated with the hyper-elastic material M4.

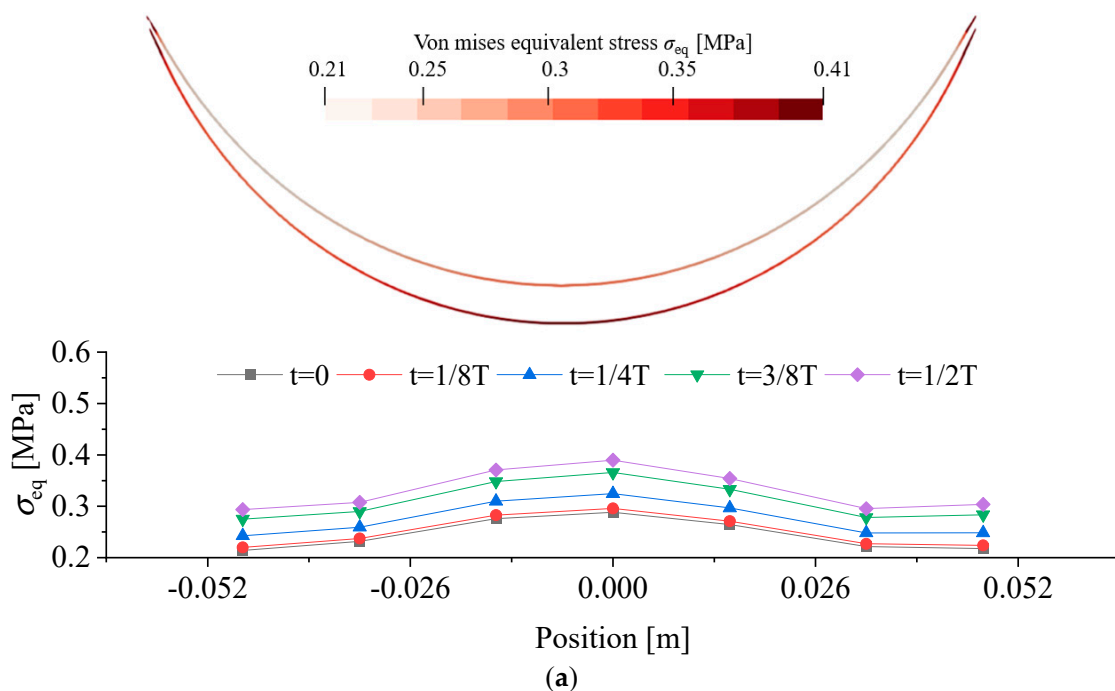


Figure 17. Cont.

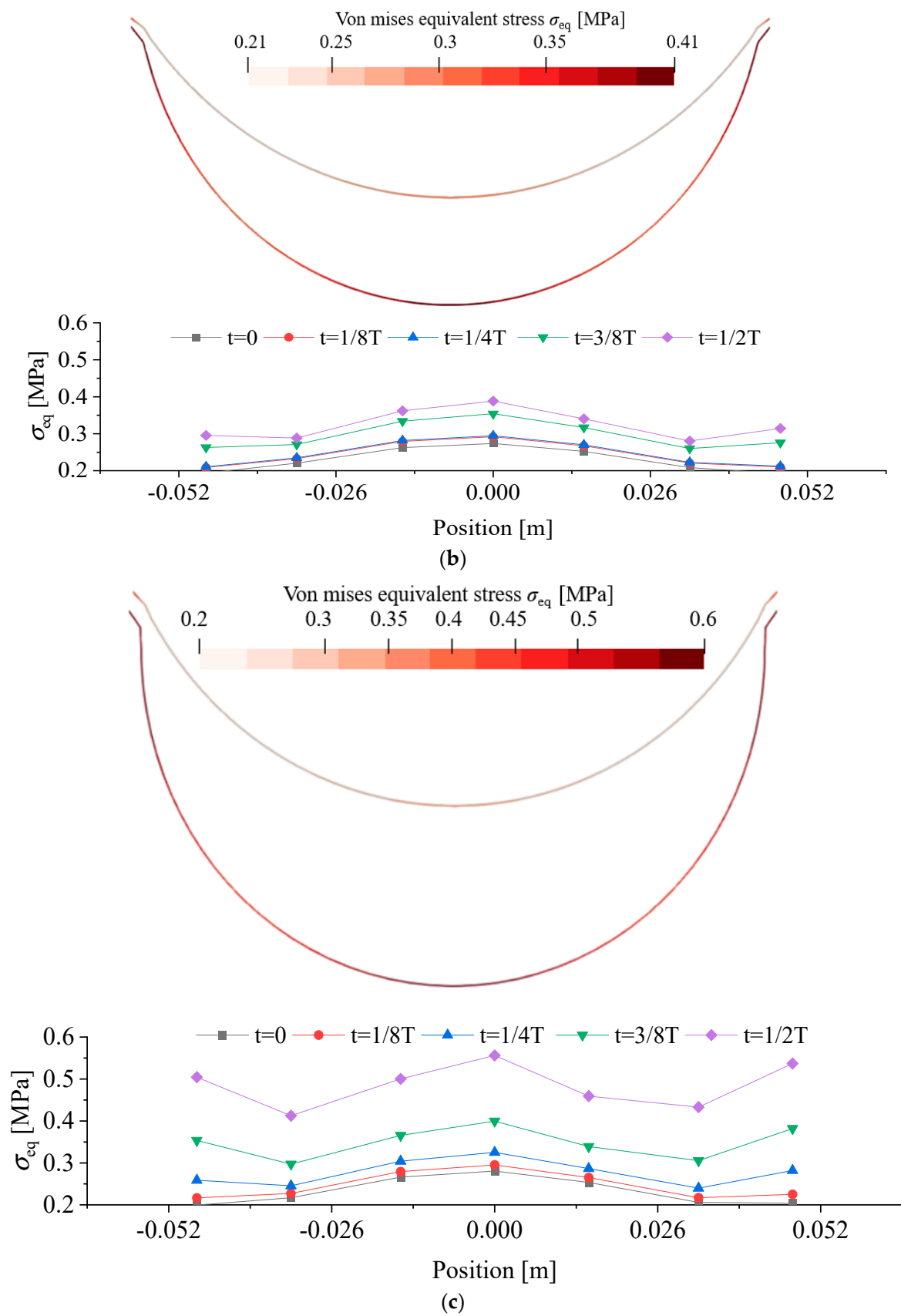


Figure 17. The maximum and minimum deformations of the membrane and the distribution of equivalent stress σ_{eq} along the membrane: (a) linear-elastic, (b) hyper-elastic M3, and (c) hyper-elastic M4 materials.

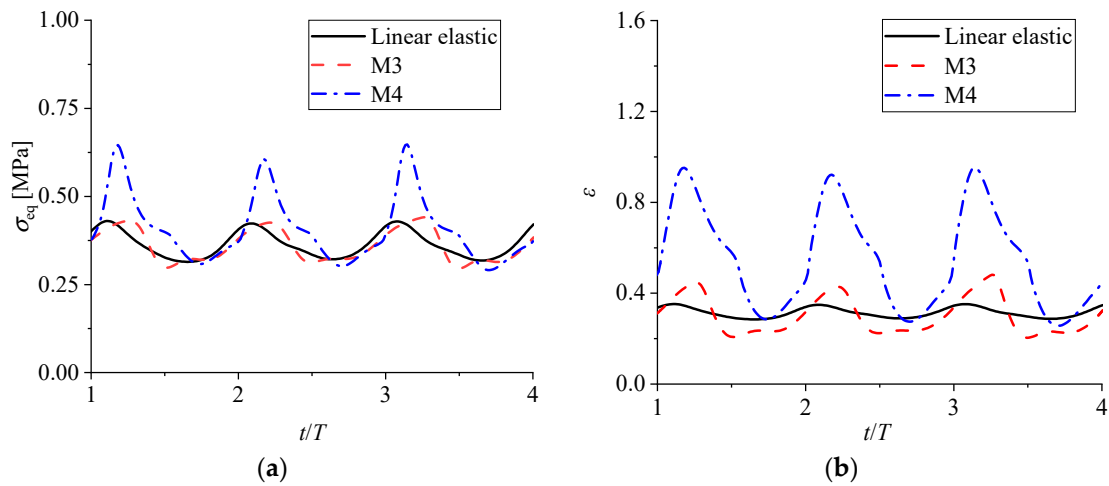


Figure 18. Time history of the variation of (a) stress σ_{eq} and (b) strain τ of the tip for different materials.

Another important feature that can be seen in Figure 17 is that the stress was non-uniformly distributed along the membrane. As expected, the maximal stress occurred both at the tip of the membrane and the far ends of the membrane, and the non-uniformity increases with the softer material from M3 to M4. This impaired the durability of the membrane, which may have been caused by the device structure fatigue.

As discussed earlier, in the design phase of the fWEC, a large motion amplitude is expected to attain better performance via the selection of different materials. Figure 19 demonstrates the effective deformation ability (the amplitude of the deformation, rather than the total deformation) associated with the material properties. The boxes are the effective stress range (ESR), which represents the actual ranges of stress and strain variation during an operation. It can be seen that the ESR of the linear-elastic material was very small, while the hyper-elastic material reached a larger value. This provides the evidence to conclude the superiority of hyper-elastic materials over linear elastic materials.

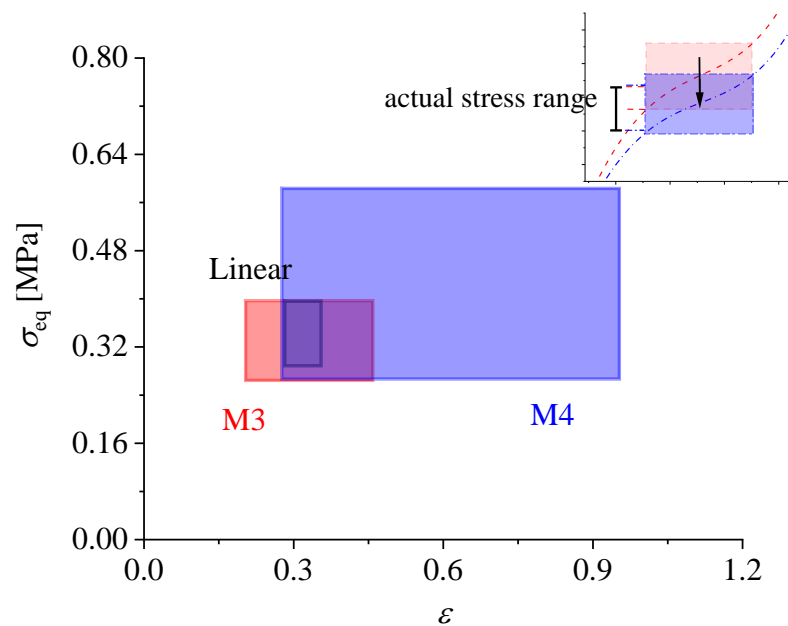


Figure 19. Effective stress range (ESR) of the fWEC. The rectangles represent the ESR of the WEC device during operation. The larger the rectangle is, the better the performance is for this material (which means a larger deformation can be achieved).

When the stiffness of M3 was reduced, the stress–strain curve translated downward, as illustrated by the zoomed-in figure at the top right. This made the ESR adapt more to the stress variation induced by the waves, thus obtaining a larger strain range and deformation. In the aspect of the practical application of material selection, if the desired deformation is predetermined, with this figure, the strain range can be estimated, and thus the material’s mechanical properties and the stress–strain relationship can be obtained.

3.5. Response of Membrane Deformation under Hydrodynamic Pressure: Wave Period Impact

The effect of the wave periods on the fWEC is studied in this section with a constant $d = 0.18$ m. The wave height was fixed to 0.1 m. The wave periods from $T = 0.8$ s to $T = 1.6$ s were studied, which corresponded to the wave periods of 5.6–12.6 s at the device’s full-scale level. The time histories for the tip displacement of the membrane are presented in Figure 20 along with the Fast Fourier Transform (FFT) analysis. In general, large wave periods led to a more vigorous motion of the membrane, indicated by the large amplitudes. For the linear-elastic material, the curve appears to have a smooth variation though some nonlinearity features that can be observed when T increases. However, given a hyper-elastic material, significant differences can be seen for $T = 0.8$ s and $T = 1.6$ s. In fact, with a large wave period, the motion was more unstable, and wavelets at the wave trough and crest can be observed, implying higher-order components were excited, which is clearly illustrated by the FFT analysis. In particular, only the first- and second-order harmonic components were excited for the linear-elastic material, while for the hyper-elastic materials M3 and M4, a third-order and even higher-order components were added in, caused by the nonlinearity of the material’s mechanical characteristics.

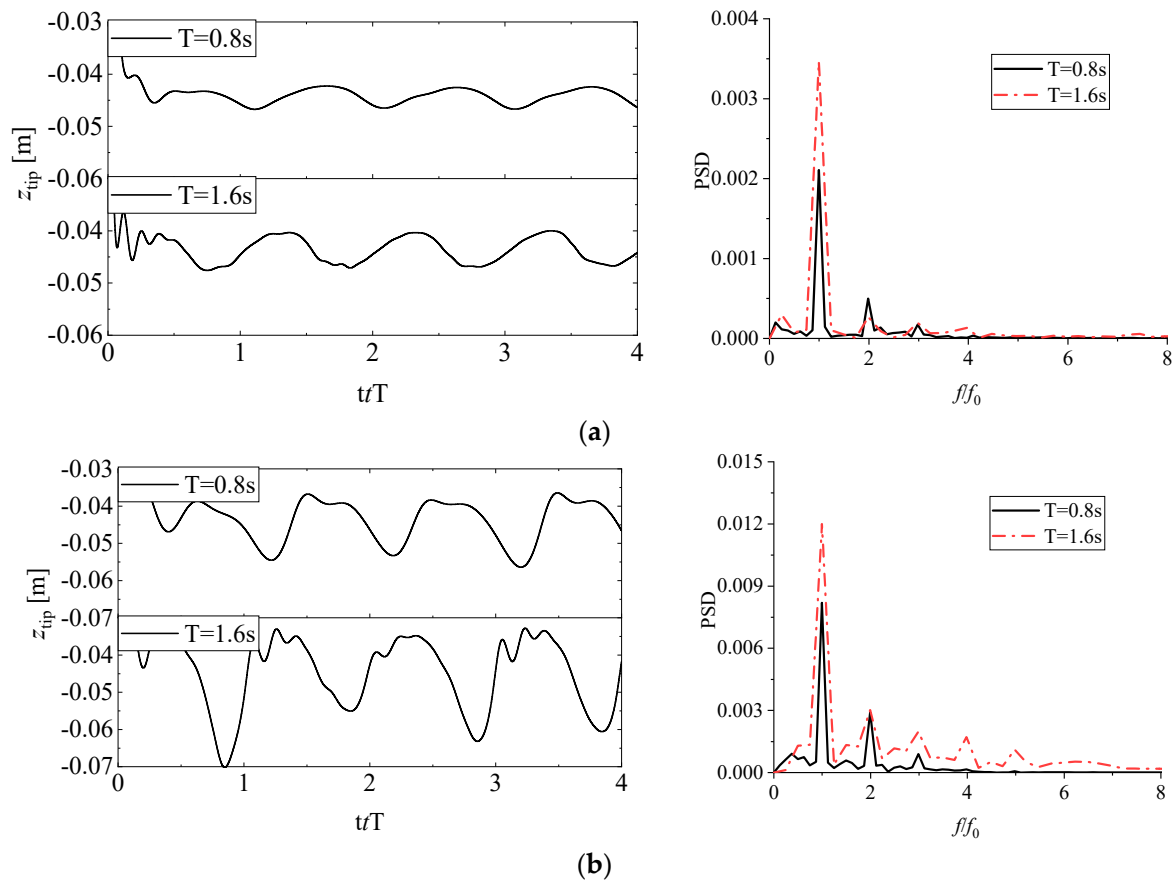


Figure 20. Cont.

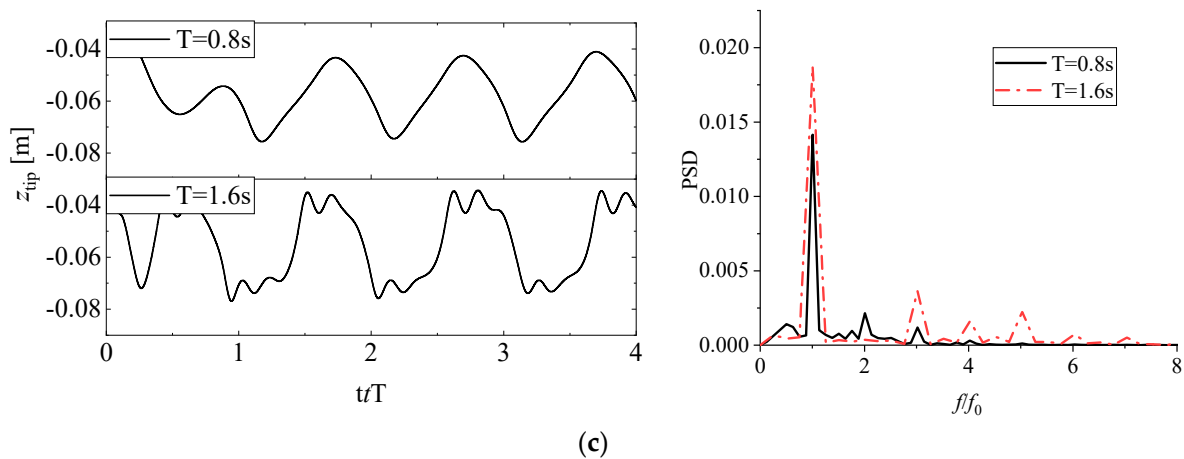


Figure 20. Time histories of the displacement of the membrane tip (left) and the FFT results (right) with (a) linear-elastic material (b) hyper-elastic M3 (c) hyper-elastic M4 ($H = 0.1\text{ m}$ and $d = 0.18\text{ m}$ for $T = 0.8\text{ s}$ and 1.6 s).

The internal flow field can be examined through the CFD results easily, and the vortex variation inside the collector is shown in Figures 21 and 22 for $T = 0.8\text{ s}$ and $T = 1.6\text{ s}$, respectively. With a wave period of $T = 0.8\text{ s}$, the clockwise and anti-clockwise vortices were generated alternately at the top left of the collector. The anti-clockwise vortex formed because of the backward flow caused by the propagating wave trough. This anti-clockwise vortex then moved downward over the fWEC, with waves passing from left to right. Meanwhile, the clockwise vortex formed due to the wave crest propagating into the water chamber. Only a clockwise vortex remained in the chamber. With a large wave period of $T = 1.6\text{ s}$, the clockwise vortex generated at the top left, and only part of the vortex went into the chamber. The vortex field was more chaotic than that of $T = 0.8\text{ s}$, and the anti-clockwise vortex remained inside. Meanwhile, the clockwise vortex generated at the top left of the chamber became larger. This contributed to the excitation of higher-order components, which partly explains why the wave with a larger period and with a smaller wave steepness showed higher nonlinearity.

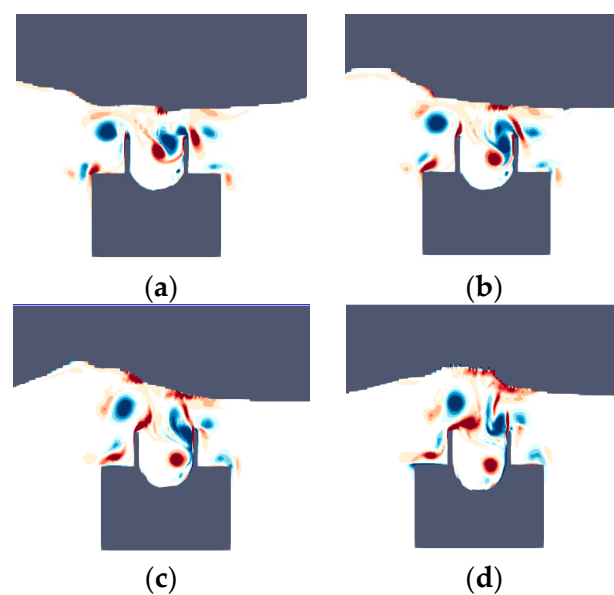


Figure 21. Cont.

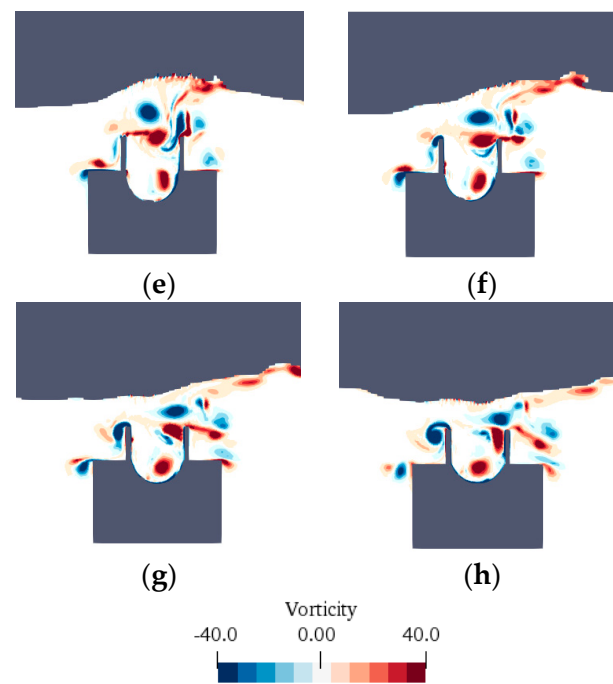


Figure 21. The instantaneous vorticity contour for $T = 0.8$ s in one wave period ($H = 0.1$ m and $d = 0.18$ m): (a) $t = 1/8T$, (b) $t = 2/8T$, (c) $t = 3/8T$, (d) $t = 4/8T$, (e) $t = 5/8T$, (f) $t = 6/8T$, (g) $t = 7/8T$, and (h) $t = 8/8T$.

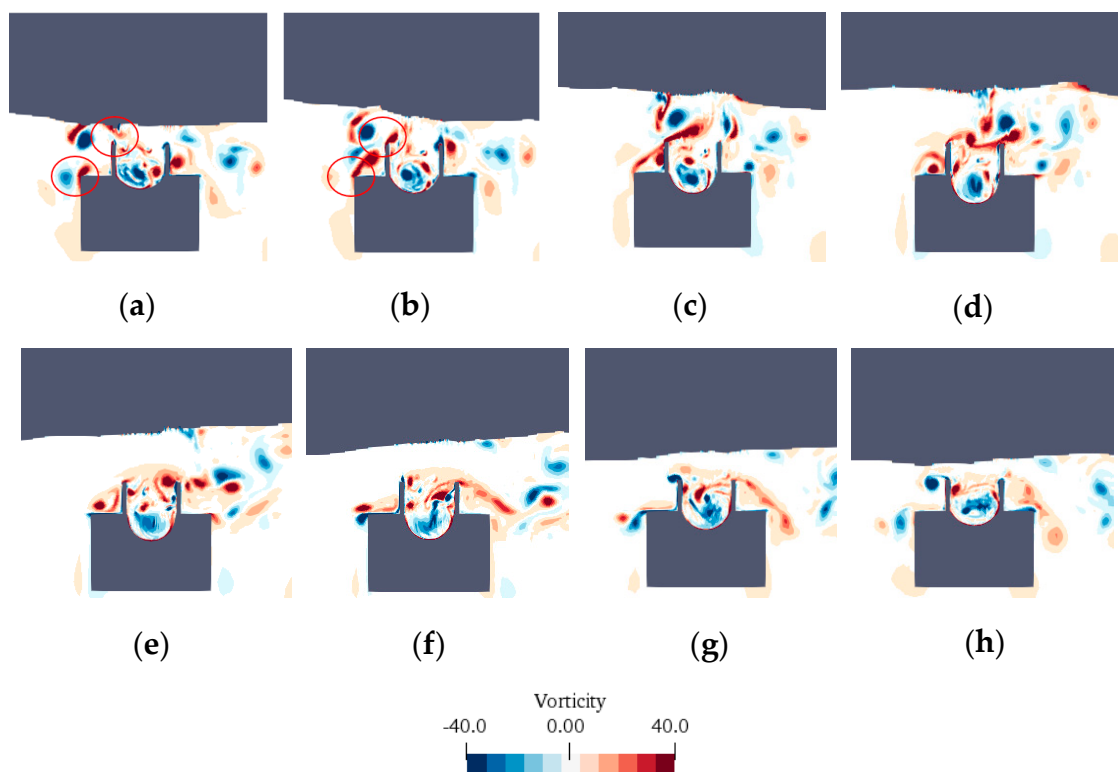


Figure 22. The instantaneous vorticity contour for $T = 1.6$ s in one wave period ($H = 0.1$ m and $d = 0.18$ m): (a) $t = 1/8T$, (b) $t = 2/8T$, (c) $t = 3/8T$, (d) $t = 4/8T$, (e) $t = 5/8T$, (f) $t = 6/8T$, (g) $t = 7/8T$, and (h) $t = 8/8T$.

The time-averaged membrane displacements with various wave periods are compared in Figure 23. Again, the hyper-elastic material had a much larger amplitude than the linear-elastic one regardless of the wave periods, indicating the advantage of using hyper-elastic material over linear material for all wave conditions. Although a subtle peak appeared between $T = 1.4$ s and $T = 1.6$ s, its magnitude was not significantly larger than those of other wave conditions. This is an advantage of the flexible WEC compared with the traditional rigid WEC. For traditional WECs, most of them usually work favorably for a specific wave condition, such as point absorber devices and OWCs. If the sea state is away from the designed wave condition, then the efficiency decreases significantly and even stops working. This was not observed in the present fWEC, which had no preference for wave conditions. As discussed in Section 3.3, the natural frequencies of the fWEC were far away from the wave frequencies, and thus there was almost no resonance occurring. However, by using a hyper-elastic material and adjusting the material parameters, a large amplitude could also be achieved without resonance, thus obtaining a large power output.

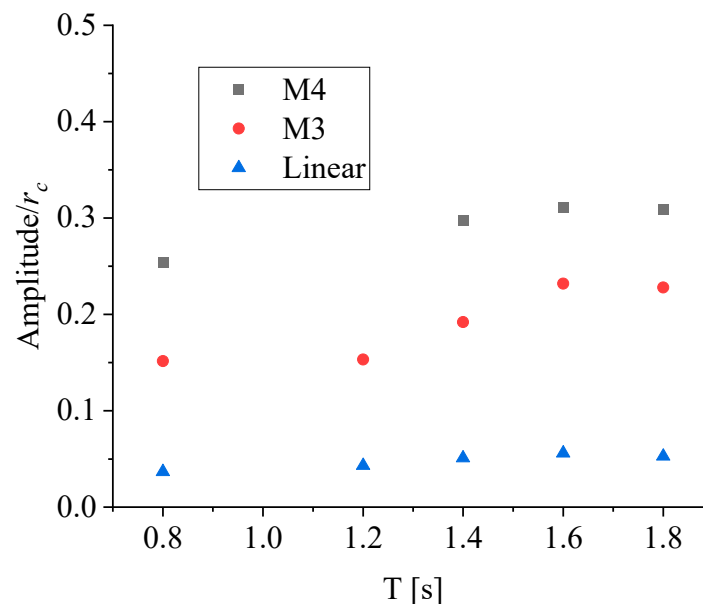


Figure 23. The amplitude of the motion for different materials versus wave period.

The power output of the fWEC at full scale was calculated via a post-process procedure using the calculated data from the CFD-FEA results. The details of the power calculation can be found in [9,41].

The electrical energy produced in one wave period can be estimated by the energy harvested from the fWEC during the charging and discharging processes:

$$E = 0.5(C_a + C_B)V_B^2 - 0.5(C_a + C_A)V_A^2 \quad (12)$$

where C_a is the additional in-parallel capacitance and V_A and V_B are the voltages immediately after the electric priming process and before the discharging process, respectively. The corresponding capacitance is C_A and C_B , which are related to the deformation of the membrane (i.e., the average thickness of the membrane t_A and t_B obtained from the simulation). The capacitance is then evaluated by the capacity equation $C_A = \varepsilon^* \varepsilon_0 S/t_A$, where ε and ε_0 are the relative dielectric constant and permittivity of vacuum, respectively, and S is the area of the membrane.

V_A and V_B can be estimated by the following equation:

$$C_A = C_a \left(\frac{V_0}{V_A} - 1 \right) \quad (13)$$

where V_0 is the priming voltage to charge the fWEC, which was 7500 V in this paper.

The calculated power output based on the above equations is summarized in Table 4. It can be concluded that the power output of the fWEC was at the level of tens of kilowatts. The performance of the fWEC significantly improved by substituting the linear-elastic material with the hyper-elastic material. The maximum power-generating capacity of M4 could be up to 112 kW. In addition, such an fWEC can effectively avoid its sensitivity to wave conditions. Indeed, as previous studies revealed, the efficiency of a conventional rigid WEC can drop significantly from 0.8 to 0.1 when the wave conditions, particularly the wave periods, are changed [5]. However, for this fWEC, the reduction in power was much less than that for rigid WECs, as indicated by the min/max power generation of 7.4/10.6 and 58.5/112.5 for the linear-elastic and hyper-elastic materials, respectively. It is worth mentioning that since the electro-mechanical model was not included in this study, the estimated power might be larger than the real values.

Table 4. Power estimation in full-scale versus varied wave period (unit: kW).

T (s)	5.6	8.4	9.8	11.2	12.6	Mean
Linear	10.6	8.2	8.7	8.7	7.4	8.7
M3	40.0	32.6	29.4	32.1	22.6	31.4
M4	112.5	81.1	79.2	72.9	58.5	80.8

4. Conclusions

This research paper studied an FSI problem of the hyper-elastic fWEC using a coupled CFD-FEA numerical tool, which is an extension of our previous study on a linear-elastic fWEC [18]. The coupled CFD-FEA numerical tool was developed, and in particular, OpenFOAM was chosen as the fluid solver, while CalculiX was selected to solve the deformation of flexible structures. Due to the fact that this study was highly nonlinear, a coupling library for multi-physics simulation (PreCICE) was implemented for robust coupling and to allow data transfer between the two solvers. With this tool, a flexible WEC with different materials used in the construction of an fWEC can be studied within a wide range of wave conditions.

The water height (d) above the PTO membrane was found to have a significant effect on the natural frequency of the fWEC. The natural frequency of the hyper-elastic fWEC was more sensitive to d , as opposed to the linear-elastic one. For both materials, the natural frequencies were found in the high-frequency region and thus away from the wave period in application scenarios. Because of this, resonance at the fundamental frequency was avoided at all stages in every case.

There existed a positive correlation between d and the deformability of the hyper-elastic fWEC; as d increased, so too did the deformation of the hyper-elastic fWEC. The linear elastic material was seen to do the opposite of this phenomenon, with the deformability getting poorer when increasing the water height d .

A further investigation of fWECs constructed with different materials indicated that the stiffness of this hyper-elastic material became smaller within a certain stress range. The hyper-elastic material became significantly less stiff. This range was given the name of the effective stress range (ESR). If the actual stress variation caused by the simulated waves matched up to the ESR, a larger level of deformability could be observed and, consequently, a larger larger generated power. By selecting the hyper-elastic material, the dynamic motion of an fWEC can be three times larger than a linear one. An adjustment of the hyper-elastic mechanical parameters can increase this ratio up to six times for the hyper-elastic material. Despite this, the stress distribution experienced along the hyper-elastic membrane is distributed unequally compared with the linear-elastic material. This makes it more vulnerable to fatigue at the tip and both ends of the membrane.

A study on how varying wave periods influenced the fWEC showed that second-order components are excited at about $T = 0.8$ s. As T increased, a greater number of higher-

order components (up to five) were excited. Although a peak period existed where the maximal motion amplitude occurred, the difference under a wide range of wave periods was insignificant. This suggests that this fWEC has strong adaptability to the sea state and does not prefer a particular wave condition to perform optimally.

Work in the future will concentrate on 3D model simulation with an acceptable time cost. In addition, a method for handling larger deformations is required, which may be solved by using the adaptive mesh or meshless methods.

Author Contributions: Conceptualization, X.L. and Q.X.; methodology, X.L.; software, X.L.; validation, X.L.; formal analysis, X.L.; investigation, X.L. and Q.X.; resources, X.L. and Q.X.; data curation, X.L.; writing—original draft preparation, X.L.; writing—review and editing, Q.X.; visualization, X.L.; supervision, Q.X.; project administration, Q.X. All authors have read and agreed to the published version of the manuscript.

Funding: This research received no external funding.

Acknowledgments: The first author thanks Giacomo Moretti from Università di Trento and Marco Fontana from Scuola Superiore Sant’Anna, who provided insight and expertise that greatly assisted this research in the field of hyper-elastic material.

Conflicts of Interest: The authors declare no conflict of interest.

References

- Henderson, R. Design, simulation, and testing of a novel hydraulic power take-off system for the Pelamis wave energy converter. *Renew. Energy* **2006**, *31*, 271–283.
- Cameron, L.; Doherty, R.; Henry, A.; Doherty, K.; Van’t Hoff, J.; Kaye, D.; Naylor, D.; Bourdier, S.; Whittaker, T. Design of the next generation of the Oyster wave energy converter. In Proceedings of the ICOE 2010 Bilbao—International Conference on Ocean Energy, Bilbao, Spain, 6–8 October 2010; p. 1e12.
- Li, X.; Xiao, Q.; Zhou, Y.; Ning, D.; Incecik, A.; Nicoll, R.; McDonald, A.; Campbell, D. Coupled CFD-MBD numerical modeling of a mechanically coupled WEC array. *Ocean. Eng.* **2022**, *256*, 111541. [[CrossRef](#)]
- Falcão, A.F.O.; Justino, P. OWC wave energy devices with air flow control. *Ocean. Eng.* **1999**, *26*, 1275–1295. [[CrossRef](#)]
- Ning, D.-Z.; Wang, R.-Q.; Zou, Q.-P.; Teng, B. An experimental investigation of hydrodynamics of a fixed OWC Wave Energy Converter. *Appl. Energy* **2016**, *168*, 636–648. [[CrossRef](#)]
- Wang, R.; Ning, D. Dynamic analysis of wave action on an OWC wave energy converter under the influence of viscosity. *Renew. Energy* **2020**, *150*, 578–588.
- Zhao, W.; Wolgamot, H.; Taylor, P.; Taylor, R.E. Gap resonance and higher harmonics driven by focused transient wave groups. *J. Fluid Mech.* **2017**, *812*, 905–939. [[CrossRef](#)]
- Yu, X.; Chwang, A.T. Wave-induced oscillation in harbor with porous breakwaters. *J. Waterw. Port Coast. Ocean. Eng.* **1994**, *120*, 125–144. [[CrossRef](#)]
- Rosati Papini, G.P.; Moretti, G.; Vertechy, R.; Fontana, M. Control of an oscillating water column wave energy converter based on dielectric elastomer generator. *Nonlinear Dyn.* **2018**, *92*, 181–202.
- Collins, I.; Hossain, M.; Dettmer, W.; Masters, I. Flexible membrane structures for wave energy harvesting: A review of the developments, materials and computational modelling approaches. *Renew. Sustain. Energy Rev.* **2021**, *151*, 111478. [[CrossRef](#)]
- Moretti, G.; Santos Herran, M.; Forehand, D.; Alves, M.; Jeffrey, H.; Vertechy, R.; Fontana, M. Advances in the development of dielectric elastomer generators for wave energy conversion. *Renew. Sustain. Energy Rev.* **2020**, *117*, 109430. [[CrossRef](#)]
- Moretti, G.; Papini, G.P.R.; Righi, M.; Forehand, D.; Ingram, D.; Vertechy, R.; Fontana, M. Resonant wave energy harvester based on dielectric elastomer generator. *Smart Mater. Struct.* **2018**, *27*, 035015. [[CrossRef](#)]
- Moretti, G.; Fontana, M.; Vertechy, R. Model-based design and optimization of a dielectric elastomer power take-off for oscillating wave surge energy converters. *Meccanica* **2015**, *50*, 2797–2813. [[CrossRef](#)]
- Michailides, C.; Angelides, D.C. Optimization of a flexible floating structure for wave energy production and protection effectiveness. *Eng. Struct.* **2015**, *85*, 249–263. [[CrossRef](#)]
- Babarit, A.; Singh, J.; Mélis, C.; Watez, A.; Jean, P. A linear numerical model for analysing the hydroelastic response of a flexible electroactive wave energy converter. *J. Fluids Struct.* **2017**, *74*, 356–384. [[CrossRef](#)]
- Farley, F.; Rainey, R.; Chaplin, J. Rubber tubes in the sea. *Philos. Trans. R. Soc. A Math. Phys. Eng. Sci.* **2012**, *370*, 381–402. [[CrossRef](#)]
- Chaplin, J.; Heller, V.; Farley, F.; Hearn, G.; Rainey, R. Laboratory testing the Anaconda. *Philos. Trans. R. Soc. A Math. Phys. Eng. Sci.* **2012**, *370*, 403–424. [[CrossRef](#)]
- Kurniawan, A.; Chaplin, J.; Greaves, D.; Hann, M. Wave energy absorption by a floating air bag. *J. Fluid Mech.* **2017**, *812*, 294–320.
- Renzi, E. Hydroelectromechanical modelling of a piezoelectric wave energy converter. *Proc. R. Soc. A Math. Phys. Eng. Sci.* **2016**, *472*, 20160715. [[CrossRef](#)]

20. Zheng, S.; Greaves, D.; Meylan, M.H.; Iglesias, G. *Wave Power Extraction by a Submerged Piezoelectric Plate*; Developments in Renewable Energies Offshore; CRC Press: Boca Raton, FL, USA, 2020.
21. King, A.; Algie, C.; Ryan, S.; Ong, R. Modelling of fluid structure interactions in submerged flexible membranes for the bombora wave energy converter. In Proceedings of the 20th Australasian Fluid Mechanics Conference, Perth, Australia, 5–8 December 2016.
22. Li, X.; Xiao, Q.; Luo, Y.; Moretti, G.; Fontana, M.; Righi, M. Dynamic response of a novel flexible wave energy converter under regular waves. In Proceedings of the 14th European Wave and Tidal Energy Conference, Plymouth, UK, 5–9 September 2021; pp. 1–7.
23. Causin, P.; Gerbeau, J.F.; Nobile, F. Added-mass effect in the design of partitioned algorithms for fluid–structure problems. *Comput. Methods Appl. Mech. Eng.* **2005**, *194*, 4506–4527. [[CrossRef](#)]
24. Bungartz, H.-J.; Lindner, F.; Gatzhammer, B.; Mehl, M.; Scheufele, K.; Shukaev, A.; Uekermann, B. preCICE—a fully parallel library for multi-physics surface coupling. *Comput. Fluids* **2016**, *141*, 250–258.
25. Jasak, H.; Jemcov, A.; Tukovic, Z. OpenFOAM: A C++ library for complex physics simulations. In Proceedings of the International Workshop on Coupled Methods in Numerical Dynamics, IUC, Dubrovnik, Croatia, 19–21 September 2007; pp. 1–20.
26. Hirt, C.W.; Nichols, B.D. Volume of fluid (VOF) method for the dynamics of free boundaries. *J. Comput. Phys.* **1981**, *39*, 201–225. [[CrossRef](#)]
27. Dingemans, M.W. *Water Wave Propagation over Uneven Bottoms: Linear Wave Propagation*; World Scientific: Singapore, 1997; Volume 13.
28. Dhondt, G. *The Finite Element Method for Three-Dimensional Thermomechanical Applications*; John Wiley & Sons: Hoboken, NJ, USA, 2004.
29. Luo, Y.; Xiao, Q.; Zhu, Q.; Pan, G. Jet propulsion of a squid-inspired swimmer in the presence of background flow. *Phys. Fluids* **2021**, *33*, 031909. [[CrossRef](#)]
30. Luo, Y.; Xiao, Q.; Shi, G.; Pan, G.; Chen, D. The effect of variable stiffness of tuna-like fish body and fin on swimming performance. *Bioinspir. Biomim.* **2020**, *16*, 016003.
31. Luo, Y.; Xiao, Q.; Zhu, Q.; Pan, G. Pulsed-jet propulsion of a squid-inspired swimmer at high Reynolds number. *Phys. Fluids* **2020**, *32*, 111901. [[CrossRef](#)]
32. Chourdakis, G.; Davis, K.; Rodenberg, B.; Schulte, M.; Simonis, F.; Uekermann, B.; Abrams, G.; Bungartz, H.-J.; Yau, L.C.; Desai, I. preCICE v2: A sustainable and user-friendly coupling library. *arXiv* **2021**, arXiv:2109.14470.
33. Degroote, J.; Bathe, K.-J.; Vierendeels, J. Performance of a new partitioned procedure versus a monolithic procedure in fluid–structure interaction. *Comput. Struct.* **2009**, *87*, 793–801. [[CrossRef](#)]
34. Haelterman, R.; Bogaers, A.E.; Scheufele, K.; Uekermann, B.; Mehl, M. Improving the performance of the partitioned QN-ILS procedure for fluid–structure interaction problems: Filtering. *Comput. Struct.* **2016**, *171*, 9–17. [[CrossRef](#)]
35. Lindner, F.; Mehl, M.; Uekermann, B. Radial basis function interpolation for black-box multi-physics simulations. In Proceedings of the International Conference on Computational Methods for Coupled Problems in Science and Engineering (COUPLED 2017), Rhodes Island, Greece, 12–14 June 2017; pp. 50–61.
36. Matthies, H.G.; Steindorf, J. Partitioned strong coupling algorithms for fluid–structure interaction. *Comput. Struct.* **2003**, *81*, 805–812. [[CrossRef](#)]
37. Wood, C.; Gil, A.; Hassan, O.; Bonet, J. Partitioned block-Gauss–Seidel coupling for dynamic fluid–structure interaction. *Comput. Struct.* **2010**, *88*, 1367–1382. [[CrossRef](#)]
38. Walhorn, E.; Hübner, B.; Dinkler, D. Space-Time Finite Elements for Fluid-Structure Interaction. In Proceedings of the PAMM: Proceedings in Applied Mathematics and Mechanics, Berlin, Germany, 25 March 2002; pp. 81–82.
39. Habchi, C.; Russeil, S.; Bougeard, D.; Harion, J.-L.; Lemenand, T.; Ghanem, A.; Della Valle, D.; Peerhossaini, H. Partitioned solver for strongly coupled fluid–structure interaction. *Comput. Fluids* **2013**, *71*, 306–319. [[CrossRef](#)]
40. Martins, P.; Natal Jorge, R.; Ferreira, A. A comparative study of several material models for prediction of hyperelastic properties: Application to silicone-rubber and soft tissues. *Strain* **2006**, *42*, 135–147.
41. Moretti, G.; Rosati Papini, G.P.; Daniele, L.; Forehand, D.; Ingram, D.; Vertechy, R.; Fontana, M. Modelling and testing of a wave energy converter based on dielectric elastomer generators. *Proc. R. Soc. A* **2019**, *475*, 20180566. [[CrossRef](#)]